We are IntechOpen,
the world's leading publisher of
Open Access books
Built by scientists, for scientists

6,900
Open access books available

185,000
International authors and editors

200M
Downloads

154
Countries delivered to

Our authors are among the

TOP 1%
most cited scientists

12.2%
Contributors from top 500 universities

BOOK CITATION INDEX
CLARIVATE ANALYTICS
INDEXED

WEB OF SCIENCE™

Selection of our books indexed in the Book Citation Index
in Web of Science™ Core Collection (BKCI)

Interested in publishing with us?
Contact book.department@intechopen.com

Numbers displayed above are based on latest data collected.
For more information visit www.intechopen.com

Data Processing Steps in Neutron Diffraction: From the Raw Data to the Differential Cross Section

J. Dawidowski[1], G. J. Cuello[2] and L. A. Rodríguez Palomino[1]

[1]*Centro Atómico Bariloche and Instituto Balseiro, Avenida Ezequiel Bustillo 9500 (R8402AGP) San Carlos de Bariloche, Río Negro*

[2]*Institut Laue Langevin, 6, rue Jules Horowitz (38042), Grenoble*

[1]*Argentina*

[2]*France*

1. Introduction

Neutron diffraction is a well established tool to investigate the structure of matter in a wide range of disciplines including Physics, Chemistry, Materials Sciences, Life Sciences, Earth Sciences and Engineering. One of its most required applications is the refinement of structures for which a considerable instrumental development has been devoted. In particular, the improvement of the instrumental resolution has been hitherto one of the main concerns in the development of the technique. In other words, most of the efforts in the instrumental development and methods has been devoted to improve the abscissas of the experimental scale (angle or momentum transfer), while on the other hand, the final results in ordinates are normally left in arbitrary units, since most of the applications do not require an absolute normalization.

Nevertheless, there is a growth in the requirements of updated neutron cross section data driven by the need of improved nuclear data libraries by Nuclear Engineers, that currently employ cross sections that sometimes are guessed or extrapolated from very old experiments. Such need could be satisfied by the highly-developed experimental neutron facilities to provide excellent quality data in absolute scales. However, this capacity remains under-exploited, as well as the procedures that are necessary to perform an absolute calibration (in the scale of ordinates), in the sense of transforming the measured number of counts into a physically meaningful scale, and expressing the final result as a cross section. This lack is closely related with the underdevelopment of data processing procedures and methods specific to each experimental configuration in neutron scattering techniques. As an example, neutron diffraction users at big facilities still employ the simple data processing correction procedures developed for X-rays techniques (Blech & Averbach, 1965; Paalman & Pings, 1962) in times when computer resources were limited. However, as shown by many reference works in the literature (Copley et al., 1986; Sears, 1975), the situation in the field of neutron scattering is far more complex, and involves the evaluation of multiple

scattering effects that can be tackled efficiently only by numerical simulations, that nowadays can be carried out with the currently available computer power.

To illustrate the consequences of this lack of a developed standard procedure to achieve an absolute normalization, let us consider the long-lasting controversy about the Hydrogen cross section for epithermal neutrons in electron-Volt spectroscopy (eVS), that began when a cross section significantly lower than commonly accepted values was reported in the literature (Chatzidimitriou-Dreismann et al., 1997), and supported by further experimental results [see e.g. (Abdul-Redah et al., 2005)]. The results stirred many criticisms, both on the theoretical likelihood of such phenomenon [see e.g. (Colognesi, 2007)], and also on the general methodology employed in the measurements and data analysis (Blostein et al., 2001) (Blostein et al., 2005). Different experiments contradicting the appearance of anomalies, employing electron-Volt spectroscopy and other techniques were also reported (Blostein et al., 2003; 2009), thus increasing the uncertainty on the matter. As an outcome of the discussion, the idea arose that the data processing methodology employed was not ready to produce a cross section in absolute units in eVs experiments. This thought led to the recent formulation of a whole body of experimental and data processing procedures (Rodríguez Palomino et al., 2011), and its application resulted in Hydrogen cross sections that are in conformity with tabulated values (Blostein et al., 2009).

In the specific case of diffraction, the problem of absolute normalization was also addressed (Rodríguez Palomino et al., 2007) following a similar approach, and the procedures were applied to a set of standard samples, measured at diffractometer D4 (ILL, Grenoble, France)(Fischer et al., 2002), and also recently to a set of light and heavy water with the aim to study the structural characteristics (Dawidowski & Cuello, 2011). The goal of the process (that will be the subject of the present work) is to provide a *modus operandi* that starts from the experimental raw data and ends in the differential scattering cross section. The starting point of the task consists in the description of the measured magnitudes through analytic expressions.

Elementary textbooks state the expressions of the measured magnitude in a diffraction experiment for point-like samples, thus finding a direct relation with the differential cross section. However, in a real experiment where extended samples are used, the formalism that describes the intensity of the scattered beam includes the sample geometry (Sears, 1975), and will be the first point to be treated. The expressions that we will show describe the measured macroscopic magnitude and its relationship with the sought microscopic differential cross section, that is not directly accessible to the experiment due to the multiple scattering, beam attenuation and detector efficiency effects. The evaluation of such effects is made through numerical simulations that follow the general guidelines stated by Copley (Copley et al., 1986). In this work we will make a detailed account of the computer code, as well as the different strategies employed to make use of the experimental data and models of interaction between the neutrons and the systems to feed the simulation program.

2. Preliminary notions

Elementary reference textbooks introduce the cross sections from a microscopic point of view (Lovesey, 1986; Squires, 1978), useful to show the link with quantum-mechanic theories. However, to make a useful comparison with experiments, the correct approach based on macroscopic magnitudes (that we will follow in this work) was formulated by Sears (Sears,

1975). We will see in this section a detail of such expressions, and their relationship with the microscopic cross sections, that is generally the sought magnitude.

2.1 Basic concepts

We will begin by considering the typical diffraction setup shown in Fig. 1, where incident neutrons are monochromatic with a wave vector $\mathbf{k}_0$ (energy E_0) and the scattered neutrons have a wavevector $\mathbf{k}$ (energy E). We will start from the *microscopic double-differential cross section* $\frac{\mathrm{d}^2\sigma}{\mathrm{d}\Omega\mathrm{d}E}$ defined in introductory textbooks as the fraction of incident neutrons scattered into the element of solid angle $\mathrm{d}\Omega$, with final energies between E and $E + \mathrm{d}E$.
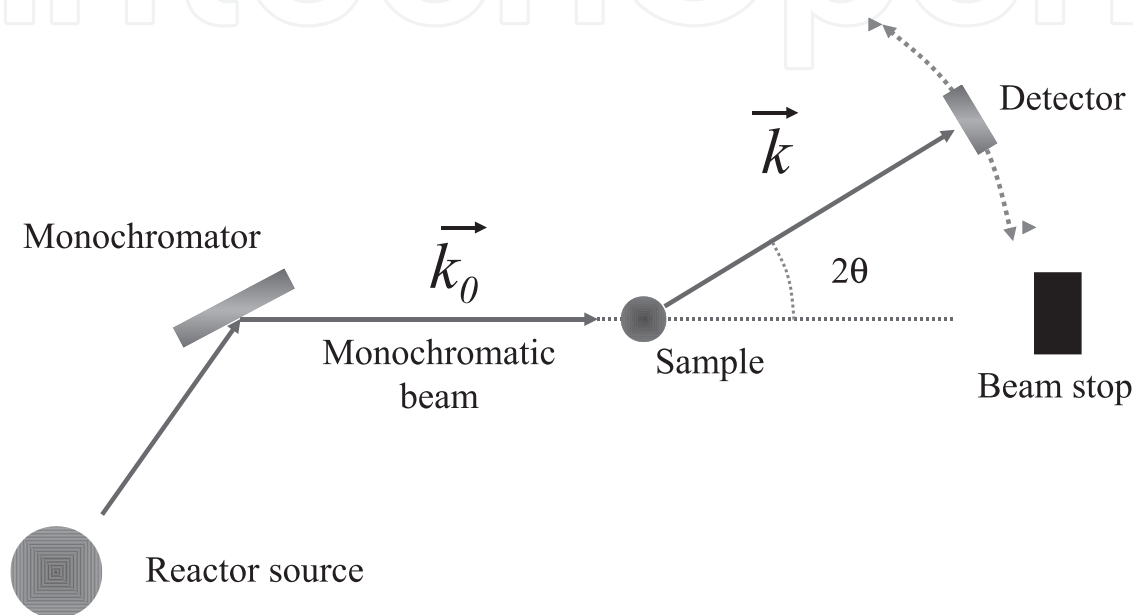

Fig. 1. Diffraction setup, showing the incident and emerging neutrons wavevectors $\mathbf{k}_0$ and $\mathbf{k}$ and the scattering angle 2θ

The microscopic integral magnitudes we will use in this work are the *differential scattering cross section*

$$\left(\frac{\mathrm{d}\sigma(E_0)}{\mathrm{d}\Omega}\right)_{\text{scatt}} = \int_{\text{all final energies}} \left(\frac{\mathrm{d}^2\sigma}{\mathrm{d}\Omega\mathrm{d}E}\right)\mathrm{d}E, \tag{1}$$

and the *total scattering cross section*

$$\sigma_{\text{scatt}}(E_0) = \int_{\text{all directions}}\int_{\text{all final energies}} \left(\frac{\mathrm{d}^2\sigma}{\mathrm{d}\Omega\mathrm{d}E}\right)\mathrm{d}\Omega\mathrm{d}E. \tag{2}$$

Normally, there are other possible contributions to the total cross section from different nuclear processes in the neutron-nucleus interaction. In this work we will consider only scattering and absorption processes, so the *total cross section* is

$$\sigma_{\text{tot}}(E_0) = \sigma_{\text{scatt}}(E_0) + \sigma_{\text{abs}}(E_0). \tag{3}$$

Both scattering and absorption components are a function of the incident neutron energy E_0. The well-known tabulated free-atom total cross section is the asymptotic value that the total cross section reaches beyond epithermal energies, as can be seen in the total cross section of Polyethylene (Fig. 2), extracted from Granada et al. (1987).
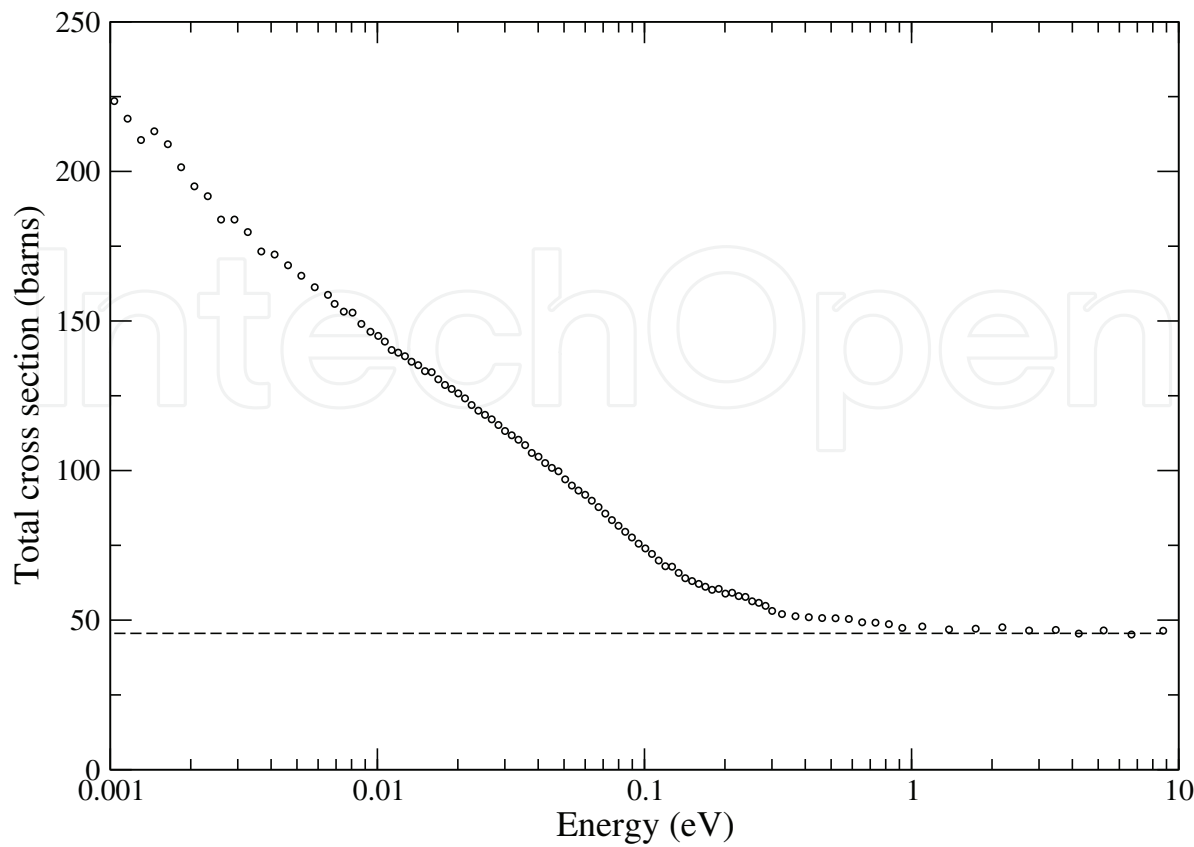
Fig. 2. Total cross section of Polyethylene (from Granada et al. (1987)) (circles). The dotted line indicates the free atom limit $2\sigma_H + \sigma_C$.

The macroscopic total cross section $\Sigma_{tot}(\mathbf{k}_0)$, is defined as

$$\Sigma_{tot}(E_0) = n\sigma_{tot}(E_0), \tag{4}$$

where n is the number density of scattering units in the sample. This magnitude describes the macroscopic aspect of the neutron interactions with the sample. For example, the probability that a neutron will interact after traversing a path x is

$$p(E_0, x) = \Sigma_{tot}(E_0) \exp(-\Sigma_{tot}(E_0)x). \tag{5}$$

Very closely related is the fraction of neutrons of a collimated beam that do not interact with the sample, called *transmission factor*, that in the case of a plane slab of thickness d is

$$t(E_0) = \exp[-\Sigma_{tot}(E_0)d]. \tag{6}$$

2.2 Cross sections for extended samples

Let us treat the case of an extended sample bathed by monochromatic neutrons (flying with velocity v_0), forming a beam of ρ neutrons per unit volume, so the flux is $\Phi = \rho v_0$ (neutrons cm^{-1} sec^{-1}). The distribution function of the incident beam can be represented as

$$f_{inc}(\mathbf{r}, \mathbf{k}) = \rho\delta(\mathbf{k} - \mathbf{k}_0) \tag{7}$$

and the distribution of neutrons arrived at a position $\mathbf{r}$ inside the sample without interaction is (see Eq. (6))

$$f_0(\mathbf{r}, \mathbf{k}) = \rho \delta(\mathbf{k} - \mathbf{k}_0) \exp[-\Sigma_{\text{tot}}(\mathbf{k}_0) L(\mathbf{r}, \hat{\mathbf{k}}_0)]. \tag{8}$$

In this expression $L(\mathbf{r}, \hat{\mathbf{k}}_0)$ is the distance from point $\mathbf{r}$ (inside the sample), to the sample surface in the direction $-\hat{\mathbf{k}}_0$.

To describe the distribution of scattered neutrons effectively observed in an experiment, the double differential-cross section (which is a microscopic concept) must be replaced by the *macroscopic double-differential cross section*, defined as the number of neutrons that *emerge from the sample* with a momentum between $\mathbf{k}$ and $\mathbf{k} + d\mathbf{k}$ of, per unit incident flux.

$$\frac{\mathrm{d}^2\Sigma}{\mathrm{d}\Omega \mathrm{d}E} = \left[\frac{mk^2}{\rho\hbar^2 k_0} \int_{S(\hat{\mathbf{k}})} \mathrm{d}S\, \hat{\mathbf{e}} \cdot \hat{\mathbf{k}} f(\mathbf{r}, \mathbf{k}) \right]. \tag{9}$$

where m is the neutron mass and the integral is performed on $S(\hat{\mathbf{k}})$, the surface of the sample that is visible from direction $\hat{\mathbf{k}}$ and $\hat{\mathbf{e}}$ is its normal unit vector. From this equation, we can derive that the expression for $\mathrm{d}^2\Sigma/\mathrm{d}\Omega \mathrm{d}E$ per unit cross sectional area exposed at the incident beam $A(\hat{\mathbf{k}}_0)$, can be decomposed in a transmitted beam plus a distribution of scattered neutrons

$$\frac{1}{A(\hat{\mathbf{k}}_0)} \frac{d^2\Sigma}{d\Omega dE} = \mathcal{T}(k_0) + \mathcal{S}(\mathbf{k}_0, \mathbf{k}), \tag{10}$$

with

$$\mathcal{T}(k_0) = \frac{mk_0}{\hbar^2} t(k_0)\delta(\mathbf{k} - \mathbf{k}_0) \tag{11}$$

and

$$\mathcal{S}(\mathbf{k}_0, \mathbf{k}) = \frac{V}{A(\hat{\mathbf{k}}_0)} \frac{n\sigma_s}{4\pi} \frac{k}{k_0} s(\mathbf{k}_0, \mathbf{k}). \tag{12}$$

In Eq. (12) σ_s is the bound-atom scattering cross section of the sample and V its volume.

The transmission factor, introduced for plane slabs in Eq. (6), for general geometries can be expressed alternatively either as a volume or a surface integral, as

$$\begin{aligned} t(k_0) &= \frac{1}{A(\hat{\mathbf{k}}_0)} \int_{S(\hat{\mathbf{k}})} \mathrm{d}S\, \hat{\mathbf{e}} \cdot \hat{\mathbf{k}}_0\, \exp[-\Sigma_{\text{tot}}(\mathbf{k}_0) L(\mathbf{r}, \hat{\mathbf{k}}_0)] \\ &= 1 - \frac{\Sigma_{\text{tot}}(\mathbf{k}_0)}{A(\hat{\mathbf{k}}_0)} \int_V \mathrm{d}\mathbf{r}\, \exp[-\Sigma_{\text{tot}}(\mathbf{k}_0) L(\mathbf{r}, \hat{\mathbf{k}}_0)]. \end{aligned} \tag{13}$$

The second term in Eq. (10) contains the effective scattering function $s(\mathbf{k}_0, \mathbf{k})$, that includes a component due to singly scattered neutrons in the sample $s_1(\mathbf{k}_0, \mathbf{k})$, another due to singly scattered neutrons in the container $s_C(\mathbf{k}_0, \mathbf{k})$, and a third due to multiply scattered neutrons $s_M(\mathbf{k}_0, \mathbf{k})$

$$s(\mathbf{k}_0, \mathbf{k}) = s_1(\mathbf{k}_0, \mathbf{k}) + s_M(\mathbf{k}_0, \mathbf{k}) + s_C(\mathbf{k}_0, \mathbf{k}). \tag{14}$$

Eq. (10) is the analytical expression of the number of neutrons that interact with a sample in a scattering experiment, and is the basis on which we will develop the expressions that must be compared with experiments.

3. Numerical simulations basic theory

3.1 General expressions

The task of developing analytical expressions for $s(\mathbf{k}_0, \mathbf{k})$ is involved, and does not lead to results of practical application. Far more profitable are the numerical simulations, since they allow a direct comparison with the experiment. Therefore, rather than developing the expressions for $s(\mathbf{k}_0, \mathbf{k})$ (than can be found in Sears (1975)), we will will examine the expressions that link the magnitudes calculated in simulations with the experimental count rates.

Neutrons detected in a scattering experiment generally undergo a variable number of collisions until they emerge from the sample. We will develop the expressions for the probabilities of detection of such neutrons after n collisions. Since the experiment does not discriminate the number of collisions of the detected neutrons, our task will be to assess the contributions of multiply scattered neutrons, to subtract them to the measured spectra, in order to keep the singly scattered component, that is directly related with the microscopic cross sections.

The basic interactions that will be described in this work are scattering and absorption. In the scattering interaction, the probability that a neutron changes from wavevector $\mathbf{k}_0$ to $\mathbf{k}$ is

$$P(\mathbf{k}_0, \mathbf{k}) = \frac{1}{\sigma_{\text{scatt}}(E_0)} \frac{\mathrm{d}^2\sigma}{\mathrm{d}\Omega \mathrm{d}E}. \tag{15}$$

The starting point of our numerical calculations is the probability that an incident neutron arrives to a point $\mathbf{r}$ and from that position is scattered with a final wave vector $\mathbf{k}$, based on Eqs. (5) and (15)

$$z_1(\mathbf{r}, \mathbf{k}_0, \mathbf{k}) = \underbrace{\frac{\Sigma_{\text{scatt}}(\mathbf{k}_0)}{A(\hat{\mathbf{k}}_0)} \exp[-\Sigma_{\text{tot}}(\mathbf{k}_0) L(\mathbf{r}, -\hat{\mathbf{k}}_0)]}_{\substack{\text{Prob. per unit area that the neutron} \\ \text{arrives at } \mathbf{r} \text{ and is scattered}}} \underbrace{P(\mathbf{k}_0, \mathbf{k})}_{\substack{\text{Prob. scatt.} \\ \text{distribution}}}. \tag{16}$$

Integrating (16) over all the sample volume, we get the *distribution of neutrons after the first scattering*. In the integral we employ the result of Eq. (13), thus obtaining

$$z_1(\mathbf{k}_0, \mathbf{k}) = \frac{\Sigma_{\text{scatt}}(\mathbf{k}_0)}{\Sigma_{\text{tot}}(\mathbf{k}_0)} (1 - t(E_0)) P(\mathbf{k}_0, \mathbf{k}). \tag{17}$$

We observe that $z_1(\mathbf{k}_0, \mathbf{k})$ is directly composed by a factor related with macroscopic properties, times another related with the sought microscopic scattering cross section. This magnitude, however, cannot be directly observed in the experiment since in general singly-scattered neutrons will undergo more collisions. So the *distribution of neutrons detected after the first scattering*, will be one of the components of the total detected spectrum, and its expression is based on Eq. (17), times the attenuation undergone by the neutron beam in the outgoing path in the sample towards the detector, times the probability that the neutron is detected (detector efficiency). The contribution from point $\mathbf{r}$ is

$$\tilde{z}_1(\mathbf{r}, \mathbf{k}_0, \mathbf{k}) = z_1(\mathbf{r}, \mathbf{k}_0, \mathbf{k}) \underbrace{e^{-\Sigma_{\text{tot}}(\mathbf{k}) L(\mathbf{r}, \hat{\mathbf{k}})}}_{\substack{\text{Attenuation} \\ \text{undergone by n in} \\ \text{the outgoing path}}} \underbrace{\varepsilon(k)}_{\substack{\text{Detector} \\ \text{efficiency}}}, \tag{18}$$

and the total contribution of the sample is the integral over all the volume

$$\tilde{z}_1(\mathbf{k}_0, \mathbf{k}) = \frac{1}{A(\hat{\mathbf{k}}_0)} \Sigma_{\text{scatt}}(\mathbf{k}_0) P(\mathbf{k}_0, \mathbf{k}) \varepsilon(k) \underbrace{\int_V d\mathbf{r}\, e^{-\Sigma_{\text{tot}}(\mathbf{k}_0) L(\mathbf{r}, -\hat{\mathbf{k}}_0)} e^{-\Sigma_{\text{tot}}(\mathbf{k}) L(\mathbf{r}, \hat{\mathbf{k}})}}_{V H_1(\mathbf{k}_0, \mathbf{k})}, \qquad (19)$$

where $H_1(\mathbf{k}_0, \mathbf{k})$ is the primary attenuation factor defined by Sears (1975).

This magnitude is directly related with $s_1(\mathbf{k}_0, \mathbf{k})$ of Eq. (14) through

$$\tilde{z}_1(\mathbf{k}_0, \mathbf{k}) = \frac{N\sigma_{\text{bound}}}{4\pi A(\hat{\mathbf{k}}_0)} \frac{k}{k_0} \varepsilon(k) s_1(\mathbf{k}_0, \mathbf{k}), \qquad (20)$$

The expression of the *distribution of neutrons detected after the n-th scattering*, $\tilde{z}_n(\mathbf{k}_0, \mathbf{k})$ is mathematically involved and will be omitted. Its calculation will be done with numerical simulations.

3.2 Application for diffraction experiments

In the case of diffraction experiments, the observed angular distributions result from the integrals in final energies of the former expressions. From Eq. (12)

$$\frac{1}{A(\hat{\mathbf{k}}_0)} \left(\frac{d\Sigma}{d\Omega}\right)_{\text{scatt}} = \frac{V}{A(\hat{\mathbf{k}}_0)} \frac{n\sigma_s}{4\pi} \int dE \frac{k}{k_0} s(\mathbf{k}_0, \mathbf{k}). \qquad (21)$$

The equivalent angular magnitudes (17) and (19) are

$$z_1(\mathbf{k}_0, \theta) = \frac{\Sigma_{\text{scatt}}(\mathbf{k}_0)}{\Sigma_{\text{tot}}(\mathbf{k}_0)} (1 - t(E_0)) \frac{1}{\sigma_{\text{scatt}}(E_0)} \frac{d\sigma}{d\Omega}(E_0, \theta) \qquad (22)$$

$$\tilde{z}_1(\mathbf{k}_0, \theta) = \frac{V}{A(\hat{\mathbf{k}}_0)} \Sigma_{\text{scatt}}(\mathbf{k}_0) \int dE \frac{1}{\sigma_{\text{scatt}}(E_0)} \sigma(E_0, E, \theta)\, \varepsilon(E) H_1(\mathbf{k}_0, \mathbf{k}), \qquad (23)$$

where Eq. (23) is the single scattering component of Eq. (21).

4. Experimental procedure

The neutron diffraction experimental procedure was treated in detail by Cuello (2008). Since we will refer in this work to experiments performed at instrument D4 (Fischer et al. (2002)) of Institut Laue Langevin, we will draw upon its customary *modus operandi* to describe the steps of a typical diffraction experiment in a steady source.

The diffractometer D4 is essentially a two-axis diffractometer as those commonly used in powder diffraction. However two main characteristics distinguish this instrument from other powder diffractometers. First, the use of hot neutrons of energy of some hundreds of meV, which allows to reach higher momentum transfer than in a conventional thermal neutron diffractometer. Second, the collimation and evacuated tubes all along the flight path from the monochromator up to the detectors, which allows to reduce the background to extremely low level.

The epithermal neutron spectrum produced in the fission reactions is thermalised by a piece of graphite near the reactor core. This hot source, in thermal equilibrium at 2400 K, serves

to shift the Maxwellian distribution of velocities to higher energies. The extraction tube is at no more that 1 mm of the hot source to avoid the thermalisation in the heavy water. At the end of this extraction tube is located a double-focusing copper monochromator that allows to choose the incident energy or wavelength; the usual wavelengths at D4 are 0.7 and 0.5 Å. This monochromatic beam passes first through a transmission monitor (an almost transparent detector) and then is collimated by means of a series of diaphragms and silts, defining the size of the beam at the sample position. Between the monochromator and the monitor there is an evacuated tube, and the sample is located in the center of a cylindrical evacuated bell-jar. Cylindrical sample shapes are preferred, in accordance with the detector array geometry. In this case the incident beam is perpendicular to the cylinder axis. When dealing with non self-supporting samples, a vanadium cell is used as container.

The detection ensemble is composed of 9 banks of 64 ^{3}He detection cells. In front of each bank an evacuated collimation tube reduces the background produced by the bell-jar wall. The flat detection surfaces are arranged in an arc of circumference in whose center the sample is placed. The detector ensemble is moved around the sample in order to register a complete diffractogram, covering a scattering angle ranging 1 to 140°.

Besides the measurement of the sample itself, a series of ancillary measurements must be performed. The most important one is the empty (vanadium) container. The empty instrument, *i.e.,* the empty bell-jar for experiments at ambient conditions or the empty sample environment for other experiments, is the background contribution. Finally, the customary procedure to normalise the measured intensity to an absolute scale, in barns per steradian, is carried out through the measurement of a vanadium solid sample. This measurement is also used to take into account the instrumental resolution.

There are two kinds of corrections to be performed on the experimental data: one set coming from the experimental conditions and the other one from the theoretical assumptions made to derive the structure factors. There are more or less standard programs available to perform these corrections like, the code CORRECT (Howe et al. (1996)).

This program performs the main experimental corrections, such as the container (empty cell) and background subtraction (empty instrument). The knowledge of dimensions and materials of each component in the beam allows the calculation of the absorption coefficients and the extraction of the sample diffractogram. In the case of cylindrical geometry, these absorption coefficients are calculated using the Paalman and Pings corrections Paalman & Pings (1962), and the multiple scattering, is evaluated using the Blech and Averbach correction Blech & Averbach (1965), is subtracted from the experimental data.

Another instrumental parameter to take into account is the detector efficiency as a function of the neutron energy, that depends on the geometry and the filling gas pressure of the detectors. In the case of D4, it is well described by (Fischer et al. (2002))

$$\varepsilon(E) = 1 - \exp\left(-\frac{0.9599}{\sqrt{E}}\right) \tag{24}$$

The last experimental correction to perform is the correction for the instrumental resolution. Knowing the instrumental resolution, one can attempt to extract the structure factor by performing a deconvolution process, but this is a difficult task. Instead, one can measure a standard vanadium sample (an almost incoherent scatterer) which should give a flat diffractogram. In fact this diffractogram is not flat because (mainly) the resolution of the

instrument and the resolution-corrected data are obtained by taking the ratio of the sample and vanadium diffractograms. In doing this, and because the cross section of vanadium is well known, the data are also normalized to an absolute scale.

5. Numerical procedure

The probability functions shown in Section 3.1 are the expressions of the distributions followed by numerical the simulations of neutron scattering experiments we will refer to. In this section we will describe the numerical procedure employed in the simulation and the data correction analysis.

The scheme we will develop involves

- A numeric simulation program
- An iterative correction scheme
- A method to perform absolute normalizations from experimental data

We will firstly refer to the numeric simulations developed to describe diffraction experiments.

5.1 Numeric simulations

The goal of the Monte Carlo simulations is to describe the real experiment as closely as possible, to provide a means to assess the effects of

- multiple scattering
- beam attenuation
- detector efficiency
- scattering from the container

The simulations we will describe involve the incident beam and the sample-container set. We do not simulate the sample environment (collimators, bell-jar container, etc.). This background contribution is assumed to be heuristically subtracted from the experimental data. A closer simulation of the sample environment falls in the domain of instrument design, and is out of the scope of the present work.

The Monte Carlo program, is based on the method proposed by Bischoff (Bischoff (1969)) and Copley (Copley et al. (1986)). In this method, discrete neutron histories are tracked and averaged in a random walk directed by interaction probabilities obtained either by measurements or by models. In this section we will describe how neutron histories are generated, and then how they are scored and recorded, following closely the formalism developed in Sect. 3.1.

5.1.1 Neutron histories

A history consists in a trajectory of the neutron inside the sample composed by a series of scattering steps. Neutron histories are originated in a random point of the sample surface that faces the incoming beam, and consists of a series of tracks governed by the path-length estimator followed by collisions governed by a suitable angle and energy-transfer probability. A variance reduction technique is employed (following Bischoff (1969); Spanier & Gelbard (1969)) to make more efficient the process. To this end the probabilities are altered, so that the neutron never leaves the sample and never is absorbed. To compensate the biased

probabilities a weight is assigned to the event. Thus a neutron history has an initial weight 1, that decreases as the neutron progresses until it drops below a significant value. In such case the history is finished.

5.1.1.1 Path lengths

The step lengths of the trajectories are governed by the macroscopic cross sections of the traversed materials. The distance traveled by the neutron between two scattering steps is randomly drawn from the distribution

$$p(E, x) = \frac{\Sigma_{\mathrm{tot}}(E, x) t(E, x)}{1 - t(E, d)},$$ (25)

that is the track-length distribution (5) altered , in order that the neutron never gets out of the sample. In Eq. (25) $\Sigma_{\mathrm{tot}}(E, x)$ is the macroscopic total cross section of the sample-container set, a distance x away from the neutron previous scattering position, taken in the current flight direction, $t(E, x)$ is the fraction of transmitted neutrons in that direction after traversing a distance x, and d is the distance to the sample surface in that direction.

As mentioned above, the neutron is also forced to scatter (since absorption is forbidden in this altered scheme). To compensate the biases in the probability, a weight is assigned to each neutron that decreases according to the transmitted fraction in the traversed path, being 1 the initial value. Given the weight at step $i - 1$ the weight at step i is calculated as in Spanier & Gelbard (1969)

$$w_i = w_{i-1}(1 - t(E, d)) \frac{\Sigma_{\mathrm{scatt}}(E, 0)}{\Sigma_{\mathrm{tot}}(E, 0)},$$ (26)

where the ratio $\Sigma_{\mathrm{scatt}}(E, 0)/\Sigma_{\mathrm{tot}}(E, 0)$ of the macroscopic scattering and total cross sections, at position $i - 1$ indicates the probability that the neutron will not be absorbed, and $1 - t(E, d)$ the probability that it will interact in the considered path. A history is finished when the weight drops under a predetermined cut-off value, so the number of scattering events is not predetermined.

To evaluate (25) and (26) the program requires as input the tabulated values of the macroscopic total cross sections of the sample and container materials, as well as their absorption probabilities as a function of energy. In Fig. 3 we show the input values employed for the case of a D_2O sample, with a vanadium cell as container. We observe the macroscopic cross section of D_2O (taken from Kropff et al. (1984)) and V (from Schmunk et al. (1960)), and the typical "$1/v$" absorption cross sections taken from Mughabghab et al. (1984).

5.1.1.2 Direction and energy after a collision

After a collision, a new energy and flight direction must be assigned for the next step in the neutron history. If E_i is the energy before the collision, the final energy E_{i+1} and the collision angle θ, must be drawn from the two-variable probability density (15), that can be rewritten as

$$P(E_i, E_{i+1}, \theta) = \frac{1}{\sigma_{\mathrm{scatt}}(E_i)} \sigma(E_i, E_{i+1}, \Omega).$$ (27)
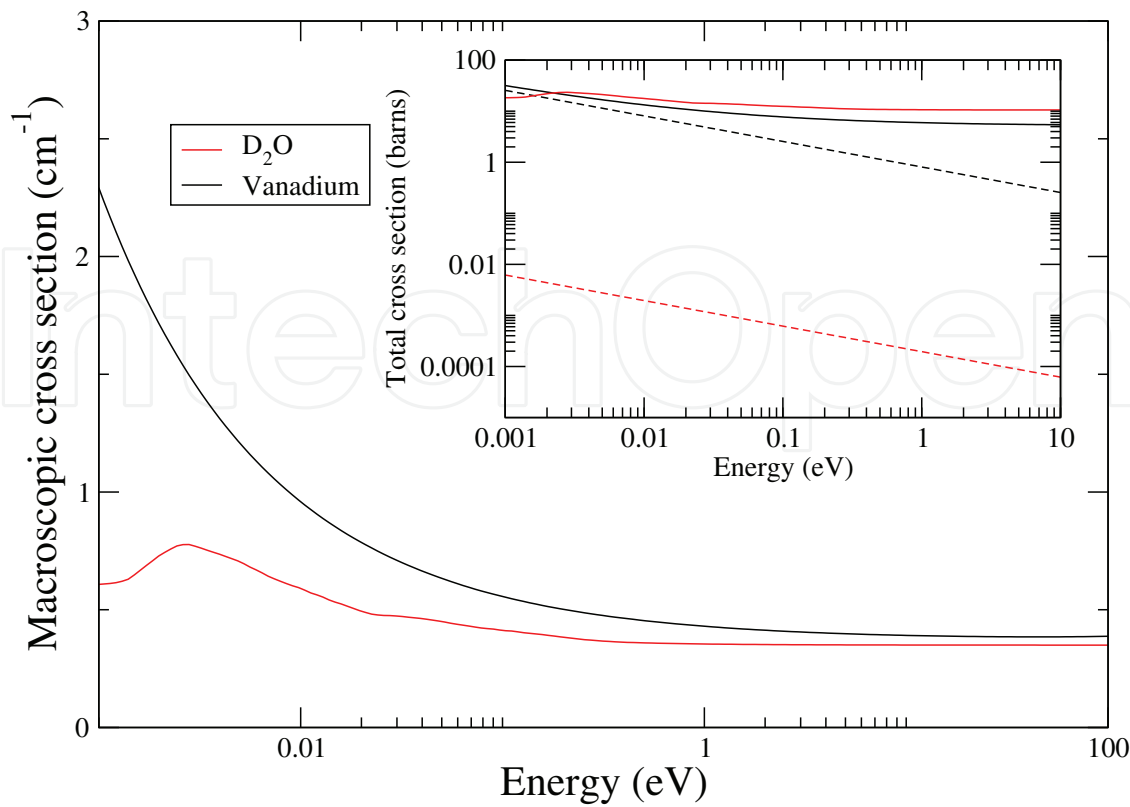
Fig. 3. Input parameters employed in the simulation of a D_2O sample, in a vanadium container. In the main frame, the macroscopic total cross sections of D_2O (after Kropff et al. (1984)) and the vanadium cross section (after Schmunk et al. (1960)). Inset: The microscopic total and absorption cross sections (Mughabghab et al. (1984)).

The process must be done in two steps (Spanier & Gelbard (1969)). First we define the marginal density as the angular integral

$$P_1(E_i, E) = \frac{1}{\sigma_{\text{scatt}}(E_i)} \int \sigma(E_i, E, \Omega) \mathrm{d}\Omega \tag{28}$$

that for the special case of systems with azimuthal symmetry (such as liquids) can be written as

$$P_1(E_i, E) = \frac{1}{\sigma_{\text{scatt}}(E_i)} \int_0^{2\pi} 2\pi \sin\theta \sigma(E_i, E, \theta) \mathrm{d}\theta. \tag{29}$$

The integral in angles is known as the *energy-transfer kernel* $\sigma(E_i, E)$ (Beckurts & Wirtz (1964)), so

$$P_1(E_i, E) = \frac{1}{\sigma_{\text{scatt}}(E_i)} \sigma(E_i, E). \tag{30}$$

The energy E_{i+1} is drawn solving the equation

$$\rho_1 = \int_{-\infty}^{E_{i+1}} P_1(E_i, E) \mathrm{d}E, \tag{31}$$

where ρ_1 is a random number uniformly distributed between 0 and 1. In the second step, the angle is defined with the probability (27), with E_i and E_{i+1} as fixed values and a second random number

$$\rho_2 = \frac{1}{\sigma_{\text{scatt}}(E_i)} \int_0^{\theta_1} 2\pi \sin\theta \, \sigma(E_i, E_{i+1}, \theta) \mathrm{d}\theta. \tag{32}$$

Since diffraction experiments do not provide a measurement of energy transfers we must rely on models to evaluate $P(E_i, E_{i+1}, \theta)$ for the different materials composing the sample. For molecular systems the Synthetic Model formulated by Granada (Granada (1985)) proved to be an adequate description for the energy transfer kernels and total cross sections. The model requires a minimum input dataset to describe the molecular dynamics, and is fast and amenable to be included in a calculation code. Since the model describes only the incoherent cross section, it is not adequate to describe the coherence manifested in the angular distributions, but is still a good description of the energy transfers, as tested in the calculation of spectra from moderators. Thus, the energies drawn through Eq. (31) can be computed with this model. In practice, the lower and upper integration limits are placed at finite values, beyond which the contribution to the integral is negligible. In Fig. 4 we show the energy transfer kernel (multiplied by E, for practical purposes) for D_2O from the Synthetic model. In yellow dashed curves we show the integration limits as a function of the incident energy employed in the calculations. The curves are calculated previously and used also as input for the simulation program, together with the input parameters of the Synthetic Model. A
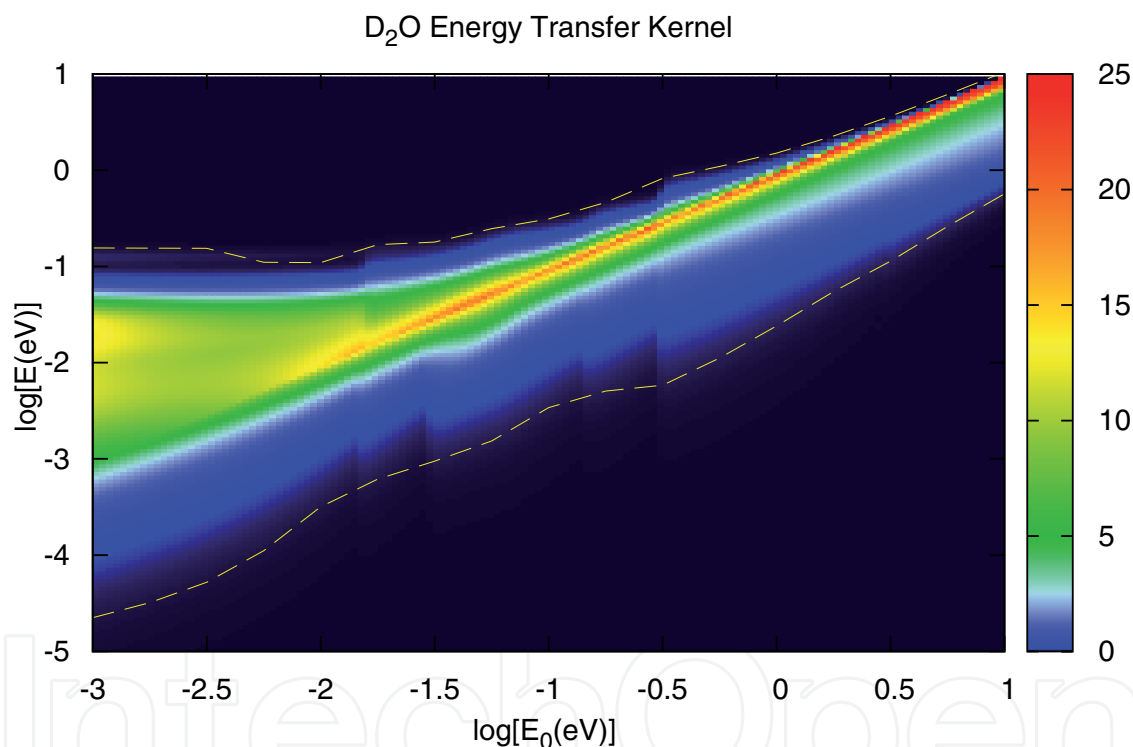

Fig. 4. Energy-transfer kernel $E\sigma(E_i, E)$ for D_2O calculated with Granada's Synthetic Model. Yellow dashed curves show the lower and upper integration limits employed in Eq. (31). The colored scale represents the intensity in barns.

basic input data table of the Synthetic Model for D_2O is shown in Table 1. The data include the energies of the oscillators $\hbar\omega_i$ and their widths $\hbar\sigma_i$ describing the molecular vibrational modes, the vibrational masses, the bound and absorption cross sections of the atoms, their masses, and the chemical composition of the molecule.

To draw angles from Eq. (32) we can follow two alternative procedures. The first is to employ also the Synthetic Model, that describes only incoherent effects as mentioned above, so it will have a narrow range of applicability, as was described by Rodríguez Palomino et al. (2007).

atom	$\hbar\omega_1$	$\hbar\omega_2$	$\hbar\omega_3$	$\hbar\omega_4$	M_1	M_2	M_3	M_4
D	14	50	150	306	40	5.2	12.1	5.87
O					40	214	290	169

atom	$\hbar\sigma_1$	$\hbar\sigma_2$	$\hbar\sigma_3$	$\hbar\sigma_4$	σ_{bound}	σ_{abs}	M atom	Numb.
D	1	21	18	19	7.63	8.2×10^{-5}	2	2
O					4.234	3.0×10^{-5}	16	1

Table 1. Values of the parameters of the Synthetic Model for D_2O used in the calculations (Granada (1985)). Energies ($\hbar\omega_i$ and $\hbar\sigma_i$) are given in meV, masses (M_i,M atom) in neutron mass units and cross sections (σ_{bound} and σ_{abs}) in barns. "Numb." indicates the number of atoms per molecule.

The second alternative is to employ the angular distributions determined by the experimental data, as will be described in this work.

The experimental data $\mathcal{E}^{(0)}(\theta)$ are usually tabulated in the elastic-Q scale,

$$Q_{\text{el}} = 2k_0 \sin(\theta/2), \tag{33}$$

where θ is the angle between the incident beam and the sample-detector path. However a Q_{el}-bin collects also all the inelastic contributions, from different initial and final energies. A practical approach in the application of Eq. (32), is to replace $\sigma(E_i, E_{i+1}, \theta)$ by a function based on the experimental data $f(\theta)$

$$f(\theta) = N\,\mathcal{E}^{(0)}(Q_i(\theta)), \tag{34}$$

where

$$Q_{\text{i}}(\theta) = 2k_i \sin(\theta/2), \tag{35}$$

and N is a normalization constant. This approach involves the idea that the angular distribution for a specific inelastic interaction is the same as the total measured distribution for elastic and inelastic processes. This question is further discussed in Sect. 7. In Fig. 5 we show the experimental data from a diffraction experiment on D_2O at D4. The raw data and and background measured with the empty bell-jar commented in Sect. 4 are shown, together with the data after background subtraction, in Q_{el} scale. The main experimental parameters are summarized in table 2.

Parameter	Value
Incident energy	324.3 meV
Beam height	5.0 cm
Beam width	0.6 cm
Cell external diameter	0.6 cm
Cell internal diameter	0.58 cm

Table 2. Experimental parameters related to the beam and sample size of the diffraction experiment in D_2O taken as example.

The justification to employ this hybrid model is that diffraction data provide an excellent approximation to the real angular distributions, while the Synthetic Model proved to be an adequate description for the energy transfer kernels for a wide variety of samples. Even in the case of coherent scatterers, the model was able to reproduce moderator spectra and the inelastic pedestal in diffraction experiments Granada (1985).
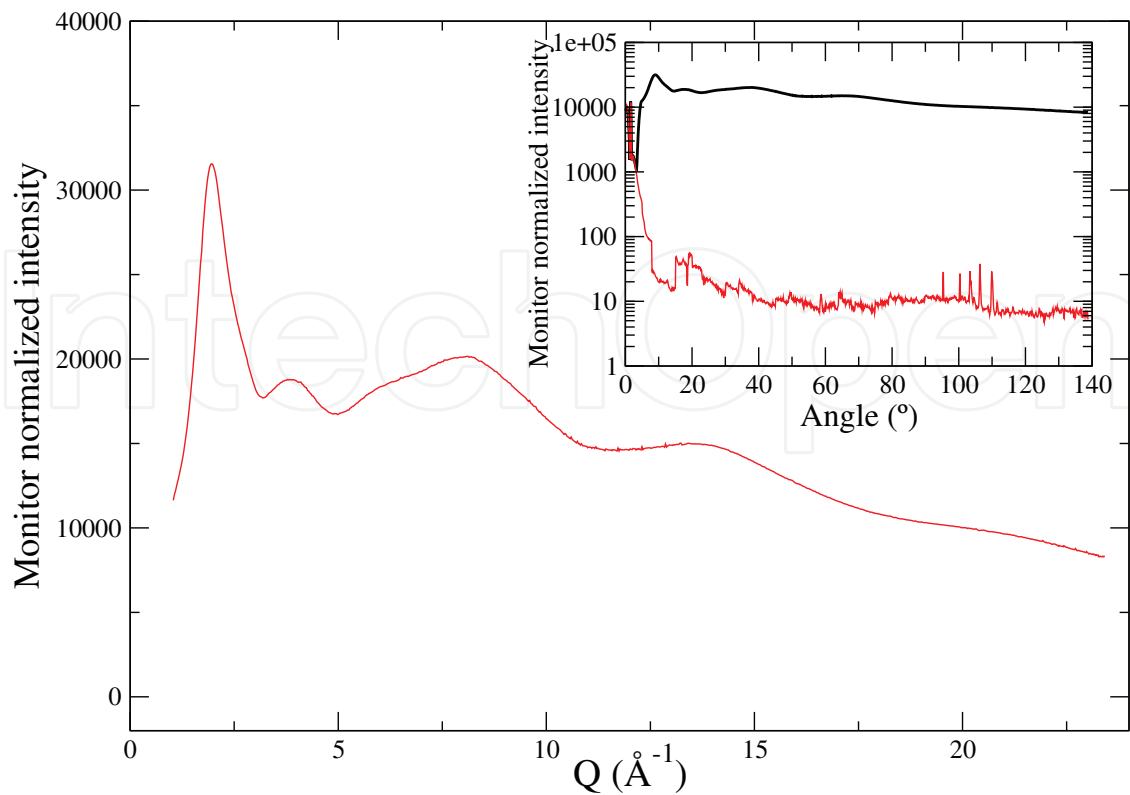
Fig. 5. Experimental data from a neutron diffraction experiment on D_2O in a vanadium container. Inset: Raw data and background measured with the empty bell-jar. Main frame: Experimental data after background subtraction, in Q_{el} scale.

Finally, if the scattering process takes place in the container, a gas model is assumed. The assumption is a good approach, since a heavy gas describes mostly elastic processes, that is a good description of the actual interactions taking place.

5.1.2 Scoring

At each step, the contribution of the current history to the final spectrum is scored for the set of detectors that compose the bank. For a detector placed at an angle θ with respect to the incident beam (taken as the z axis), with a direction characterized by the unit vector $\hat{\mathbf{d}} = (0, \cos\theta, \sin\theta)$, and if the neutron is flying inside the sample in the direction $\hat{\mathbf{k}} = (k_x, k_y, k_z)$, the scattering angle ϕ of the neutron to the detector position is calculated trough

$$\cos\phi = k_y \cos\theta + k_z \sin\theta \tag{36}$$

The scored magnitudes are summarized in table 3

Estimator	Description
$z_1(\mathbf{k}_0, \theta)$	Singly scattered neutrons
$\tilde{z}_1(\mathbf{k}_0, \theta)$	Detected singly scattered neutrons
$\tilde{z}_C(\mathbf{k}_0, \theta)$	Detected singly scattered neutrons from cell
$\tilde{z}_M(\mathbf{k}_0, \theta)$	Detected multiply scattered neutrons

Table 3. Estimators calculated in the numerical simulations

The contribution to the *distribution of neutrons after the first scattering* (Eq. (17)), can be obtained by scoring the estimator composed by the weight w_1 (Eq.(26))

$$z_1(\mathbf{r}_1, \mathbf{k}_0, \theta) = w_1 \mathcal{E}^{(0)}(Q),$$ (37)

where the normalized experimental angular distribution is employed as angular probability expressed in the elastic-Q scale. This scale has to be recalculated at every new neutron energy and renormalized in the accessible Q-range. It can be shown that the average over a large number of histories of (37) leads to the desired result (22). Similarly, the *distribution of detected neutrons after the i-th scattering* results from the average of the estimator

$$\tilde{z}_i(\mathbf{r}_i, \mathbf{k}_{i-1}, \theta) = w_i \mathcal{E}^{(0)}(Q) t(E_{i-1}, \mathbf{r}_i, -\hat{\mathbf{k}}) \varepsilon(E),$$ (38)

where i is the step of the history, w_i is the weight of the neutron, and $t(E_i, \mathbf{r}_i, -\hat{\mathbf{k}})$ is the transmission coefficient from the point $\mathbf{r}_i$ inside the sample to the sample surface in the direction $\hat{\mathbf{k}}$ to the detector position. The average of (38) over a large number of histories converges to (23).

As we will show in the next section the experimental $\mathcal{E}^{(0)}(Q)$ is corrected in successive runs, resulting the distribution $\mathcal{E}^{(j-1)}(Q)$ that is employed in Eqs. (37) and (38) as the experimental distributions corrected in the preceding run.

The Monte Carlo process also records the sum of multiple scattering contributions occurring either in the sample or the container

$$\tilde{z}_{\mathrm{M}}(\mathbf{r}_i, \mathbf{k}_0, \theta) = \sum_{i=2} \tilde{z}_i(\mathbf{r}_i, \mathbf{k}_0, \theta)$$ (39)

and the contribution of single-scattering events in the container $\tilde{z}_{\mathrm{C}}(\mathbf{r}_1, \mathbf{k}_0, \theta)$. The average after a large number of histories of these magnitudes are $\tilde{z}_{\mathrm{M}}(\mathbf{k}_0, \theta)$ and $\tilde{z}_{\mathrm{C}}(\mathbf{k}_0, \theta)$, *i.e.* the contribution of the multiple-scattered and container-scattered neutrons to the detected spectrum.

5.2 Iterative method

The magnitudes $\tilde{z}_1(\mathbf{k}_0, \theta)$ and $z_1(\mathbf{k}_0, \theta)$ defined in Eqs. (22) and (23) respectively can be determined with the Monte Carlo procedure, as well as $\tilde{z}_{\mathrm{M}}(\mathbf{k}_0, \theta)$ and $\tilde{z}_{\mathrm{C}}(\mathbf{k}_0, \theta)$. After the *j-th* Monte Carlo run is completed we can define the *multiple scattering factor*

$$f_{\mathrm{MS}}^{(j)}(\mathbf{k}_0, \theta) = \frac{\tilde{z}_1^{(j)}(\mathbf{k}_0, \theta)}{\tilde{z}_1^{(j)}(\mathbf{k}_0, \theta) + \tilde{z}_{\mathrm{C}}^{(j)}(\mathbf{k}_0, \theta) + \tilde{z}_{\mathrm{M}}^{(j)}(\mathbf{k}_0, \theta)},$$ (40)

and the ratio of detected singly-scattered neutrons to the total singly-scattered neutrons, which we will call *generalized attenuation factor*

$$\mathcal{A}^{(j)}(\mathbf{k}_0, \theta) = \frac{\tilde{z}_1^{(j)}(\mathbf{k}_0, \theta)}{z_1^{(j)}(\mathbf{k}_0, \theta)} = \frac{V}{A(\hat{\mathbf{k}}_0)} \frac{\Sigma_{\mathrm{tot}}(\mathbf{k}_0)}{(1 - t(E_0))} \int dE \frac{\sigma(E_0, E, \theta)}{\frac{d\sigma}{d\Omega}(E_0, \theta)} \varepsilon(E) H_1(\mathbf{k}_0, \mathbf{k}).$$ (41)

It is illustrative to point out that in the case of purely elastic scattering this magnitude is simply related with the first order attenuation factor defined in Sect. 3.1 as

$$\mathcal{A}_{\text{elast}} = \frac{V}{A(\hat{\mathbf{k}}_0)} \frac{\Sigma_{\text{tot}}(\mathbf{k}_0)}{(1 - t(E_0))} \, \varepsilon(E_0) H_1(\mathbf{k}_0, \mathbf{k}_0). \tag{42}$$

The iterative correction process consists in applying to the experimental angular distribution $\mathcal{E}^{(0)}(Q)$, the correction factors defined in Eqs. (40) and (41) after a Monte Carlo run. The angular distribution thus corrected serves as input for the next run. Thus, in the first run, the raw experimental angular distribution (background subtracted) $\mathcal{E}^{(0)}$ is employed as input, and in the run $j + 1$, we employ the distribution originated in run j as

$$\mathcal{E}^{(j+1)}(Q) = \frac{f_{\text{MS}}^{(j)}(\mathbf{k}_0, \theta) \, \mathcal{E}^{(0)}(Q)}{\mathcal{A}^{(j)}(\mathbf{k}_0, \theta)}. \tag{43}$$

The process finishes when no appreciable changes in the angular distribution are observed.

5.3 Summary of input data

Table 4 summarizes the input data required to perform a simulation of a diffraction experiment, with references to the specific example presented in this work. This set of data constitutes the minimum knowledge that must be gathered to perform the experimental program proposed in this work.

Data	Reference
Measured angular distribution, Background subtracted	Figure 5
Total cross section of the sample and the container	Figure 3
Absorption cross section of the sample and the container	Figure 3
Detector bank efficiency as a function of energy	Eq. (24)
Input parameters for the model that describes inelastic interactions	Table 1, Figure 4
Geometry parameters for the proposed experimental setup and sample environment	Table 2

Table 4. Summary of input data required in the numeric simulation of diffraction experiments. The reference indicates the specific data presented in this work.

6. Examples and applications

In this section we will show selected results of the collected experience in the application of this method (Dawidowski & Cuello (2011); Rodríguez Palomino et al. (2007)).

We begin showing diffraction experiments carried out on a series of D_2O and H_2O mixtures at room temperature, at the diffractometer D4 already mentioned in Sect. 4 (Institute Laue Langevin). We will mainly concentrate on the results for pure H_2O and D_2O. The incident neutron beam wavelength was $\lambda_0 = 0.5$ Å (energy 0.324 eV). The sample holder was a
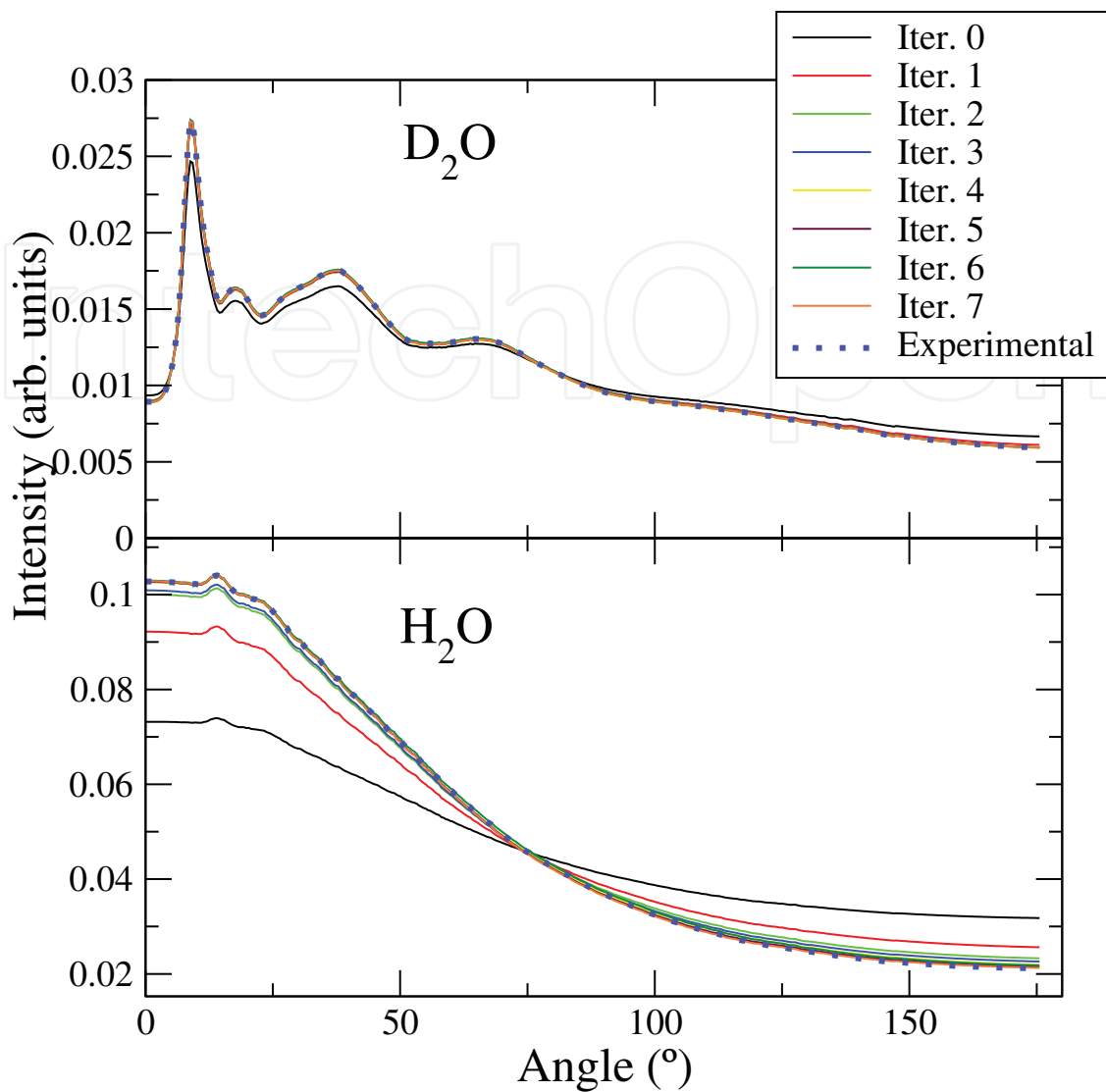
Fig. 6. Total scattering distribution calculated in successive iterations, compared with the experimental data, for D_2O and H_2O.

thin-walled cylindric vanadium can, 6 mm inner diameter and 60 mm height, situated at the centre of an evacuated bell jar.

To illustrate the iterative process we compare results from pure D_2O and H_2O in Figs. 6 and 7. Fig. 6 shows the total scattering calculated in 8 iterations. In H_2O where the level of multiple scattering is higher, the total scattering calculated in the first two iterations differ substantially from the original experimental data. The reason is that the experimental data firstly employed as the input for the angular distribution, also includes the components of multiple scattering and the attenuation effects that have to be corrected. As the iterative process progresses, the corrected experimental data approach closer to the distribution of singly scattered neutrons. We observe that the convergence is achieved starting from iteration 4 in H_2O and from iteration 2 in D_2O.

The effect of the iterative process is also illustrated in Fig. 7, where we show the results on both samples in the first and eighth iterations. In the Figure, we show the distribution

Fig. 7. Calculated components of a diffractogram compared with the experimental data for D_2O and H_2O. Also shown the distribution of singly scattered neutrons $z_1(\mathbf{k}_0, \theta)$ (orange line).

of singly scattered detected neutrons $z_1(\mathbf{k}_0, \theta)$, and the contributions from the cell $z_c(\mathbf{k}_0, \theta)$ and multiple scattering $z_M(\mathbf{k}_0, \theta)$. Also shown in the same figure are the distributions of singly scattered neutrons $z_1(\mathbf{k}_0, \theta)$, that corresponds also to the corrected experimental data in the current step of iteration. As the total scattering resulting from the calculation process converges to the experimental data, the rest of the components also converge to stable values.

In Fig. 8, we show the attenuation ($\mathcal{A}^{(8)}(\mathbf{k}_0, \theta)$) and multiple scattering ($f_{MS}^{(8)}(\mathbf{k}_0, \theta)$) factors after the convergence of the process.

The conclusion of the correction process described in this work is portrayed in Fig. 9, where we show the experimental data and their corresponding corrected data.

6.1 Absolute normalization

The procedure shown in the previous sections achieves the goal to correct the experimental data for attenuation, detector efficiency and multiple scattering effects. The corrected diffractogram is thus proportional to the desired *angular distribution of singly scattered neutrons*
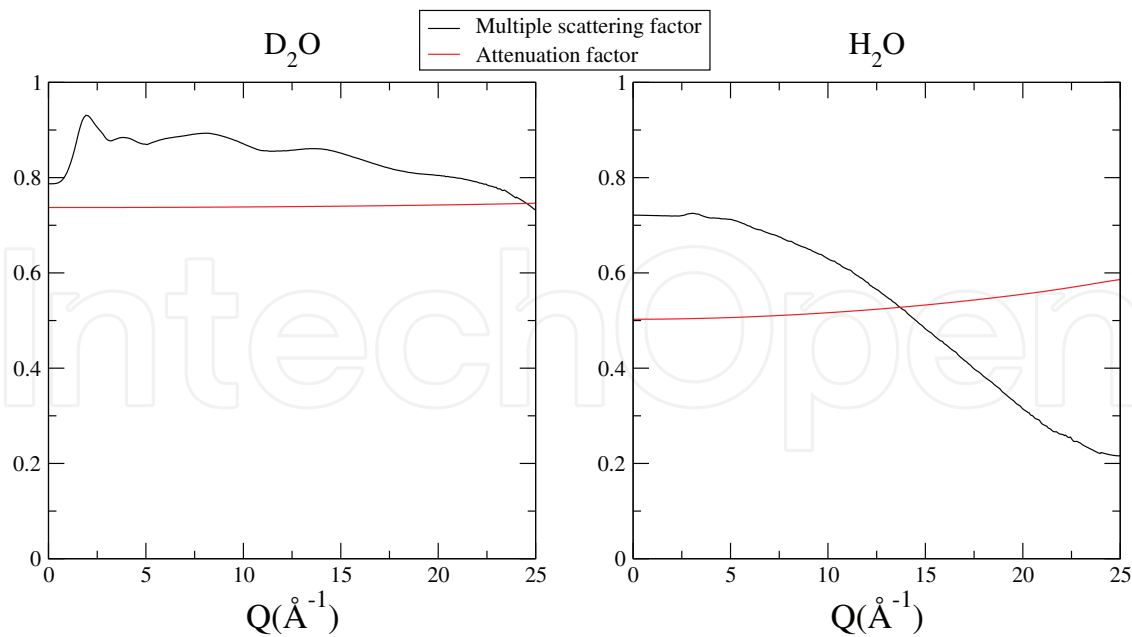
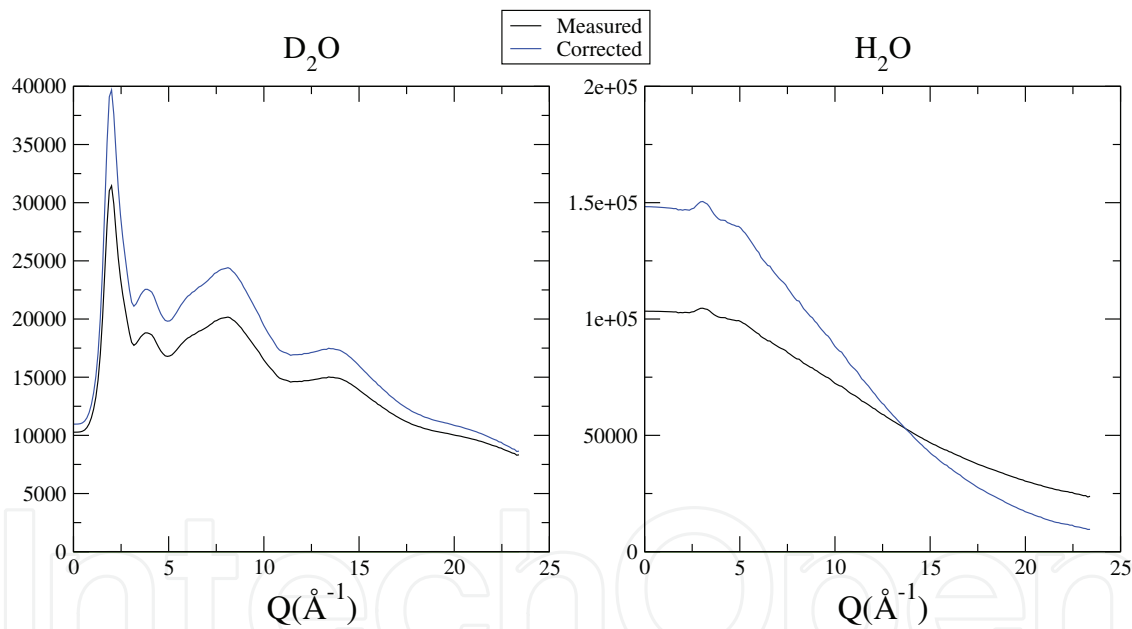Fig. 8. Attenuation factor (Eq.(41)) and multiple scattering factor (Eq. (40)) for D_2O and H_2O.

Fig. 9. Comparison between the measured and the corrected diffractograms for D_2O and H_2O after the correction procedure described in this work.

developed in Sect. 3.1. As we showed, Equation (22) is the analytic expression of this magnitude that is directly related with $d\sigma/d\Omega$, the sought result in diffraction experiments. Then,

$$Z_1^{\exp}(\mathbf{k}_0, \theta) = K z_1(\mathbf{k}_0, \theta). \tag{44}$$

The constant K encompasses experimental magnitudes that are independent of the sample, such as the intensity of the incident flux, the efficiency of the detector system, and the monitor normalization.

Fig. 10. Main frame: Values of K for the different D_2O-H_2O mixtures as a function of the scattering power of the samples. The mean K value is indicated as an horizontal dotted line. Also shown is K calculated from a vanadium rod 6 mm diameter, 6 cm height. Left inset: scattering power of the samples as a function of hydrogen concentration. Right inset: the ratio $\Sigma_{tot}(\mathbf{k}_0)/\Sigma_{scatt}(\mathbf{k}_0)$ at the incident neutron energy (324 meV) as a function of hydrogen concentration.

The value of K is obtained by integration in angles or its equivalent in Q in Eqs. (22) and (44)

$$
\begin{aligned}
K &= \frac{\Sigma_{tot}(\mathbf{k}_0)}{\Sigma_{scatt}(\mathbf{k}_0)} \frac{1}{1-t(E_0)} \int_0^{2\pi} Z_1^{exp}(\mathbf{k}_0,\theta) 2\pi \sin\theta d\theta \\
&= \frac{\Sigma_{tot}(\mathbf{k}_0)}{\Sigma_{scatt}(\mathbf{k}_0)} \frac{1}{1-t(E_0)} \int_0^{2k_0} Z_1^{exp}(\mathbf{k}_0,Q) \frac{2\pi}{k_0^2} Q dQ.
\end{aligned}
\tag{45}
$$

To perform the integral, the data must be extrapolated up to $\theta = 180^0$.

In Fig. 10 we show the values of K obtained for the the different D_2O-H_2O mixtures as a function of the scattering power of the samples. Also shown is K calculated from the diffractogram of a vanadium rod 6 mm diameter, 6 cm height (typically employed as calibrator sample), subjected to the same corrections. We observe a variation about 5% around the mean value. The reason for it will be analyzed in the next section.

The result of the calibration process is shown in Fig. 11, where the differential cross sections of D_2O and H_2O are shown expressed in barns per steradian. The data are thus properly normalized, and their integral in Q is the total cross sections an the incident neutron energy (324 meV).
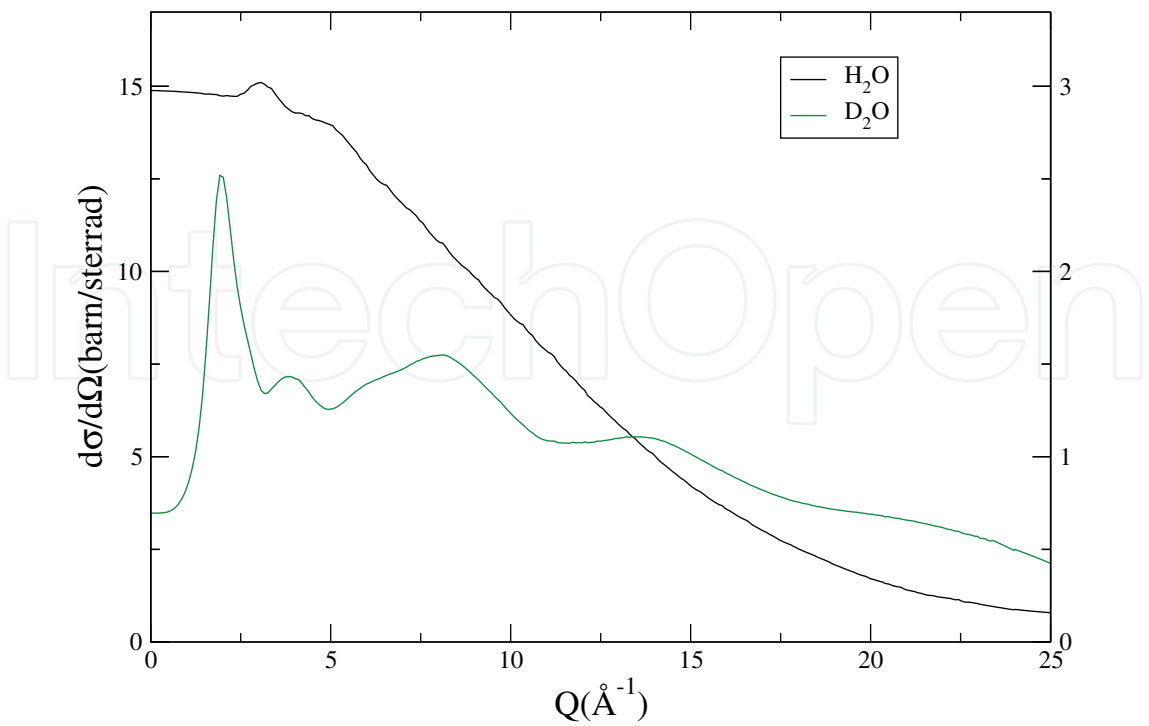
Fig. 11. Differential cross sections of D_2O and H_2O normalized with the procedure of this paper. The left y-axis corresponds to H_2O and the right y-axis to D_2O.
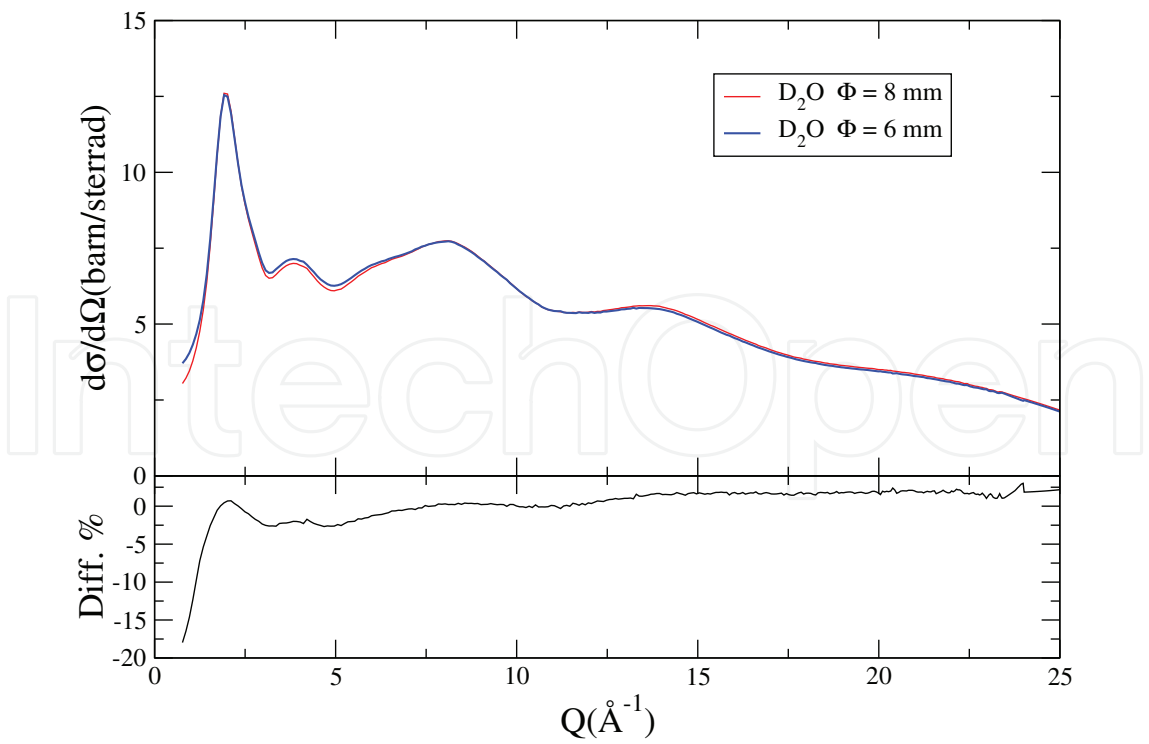

Fig. 12. Upper frame: Assessment of the data correction procedure applied to D_2O samples of different diameters. Lower frame the percentage difference.

7. Discussion

It is worth to comment about the coefficient K, the constant that links the scattering power of the samples with the number of registered counts (Eq. (44)). If the correction procedure is accurate in its different aspects, this coefficient should be an instrumental constant independent of the sample. The observed decreasing trend with the higher Hydrogen-containing samples, has been already noticed in Ref. Rodríguez Palomino et al. (2007). The causes there analyzed were possible systematic errors in the description of the detector bank efficiency, and the presence of a sample-dependent background, that increases with the higher Hydrogen-containing samples. Regarding the detector efficiency, it was exhaustively checked during the process of calibration of D4C Fischer et al. (2002). However, the sample-dependent background is a subject that remains to be treated, both from the numerical and the experimental points of view, and is not only a problem in diffraction experiments but a general issue in neutron scattering experiments.

It is interesting also to explore the limits of the present prescription by comparing the corrected data of D_2O from samples of different sizes, shown in Fig. 12. There is a general good agreement, except for the largest discrepancies shown at lower Q values, where the relative importance of the multiple scattering component is more significant. Improvements on the model should be explored regarding the angular distributions we employed, that were based on the experimental data. The present model involves the assumption that the angular distribution for inelastic processes is the same as for elastic processes. A more accurate procedure would involve a detailed knowledge of the double differential cross section of the studied material, that is normally out of the possibilities of the experimenter that performs a diffraction experiment. The present prescription is intended to keep as reasonable as possible the number of required parameters that are external to the experiment itself. A detailed assessment of this approach with a combination of diffraction and inelastic experiments, remains yet to be done, and should be left for special cases where the inelasticity plays a primary role. The convergence of the iterative process proves the self-consistency of the method. However we must be cautious, because the accuracy of its results will still depend on the goodness of the model employed to describe the system.

8. Conclusions

In this paper we showed a procedure to obtain the link between the arbitrary experimental scale in neutron diffraction experiments (number of recorded counts per monitor counts) with the corresponding cross sections that collects updated knowledge about simulations and cross sections, to describe the processes as realistically as possible. The process involves multiple scattering, attenuation and detector efficiency corrections, that are calculated by a Monte Carlo method. We also developed the mathematical expressions of the magnitudes calculated by Monte Carlo and their experimental counterparts. Those expressions link the measured macroscopic magnitudes with the sought microscopic one.

It is also important to stress that the present prescription is a step ahead over the Paalman-Pings and Blech-Averbach corrections customarily employed, that assume a model of elastic and isotropic scattering. The shortcomings of those simplified approaches compared with the present prescription was analyzed in Rodríguez Palomino et al. (2007), where differences up to 20% were found in hydrogenated samples in which the elastic isotropic model is completely inaccurate.
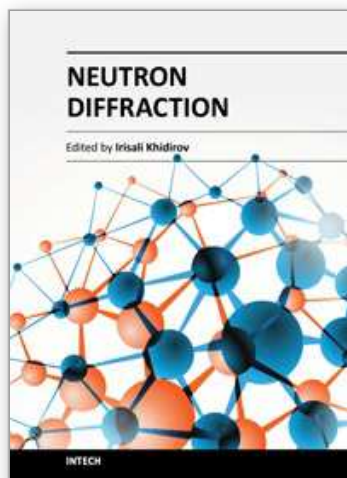
An important issue, yet to be tackled, is the role of vanadium as a normalizer. The usual measurement of a vanadium sample in D4 does not yield, in general, angular distributions according to theoretical differential cross sections (Cuello & Granada (1997)), because of the instrumental resolution effects. A complete simulation of the instruments with the available simulation software (e.g. McStas), together with the sample simulation must be the next step to solve the issue. The approach we employed in our normalization procedure based on an integral of the diffractograms, avoids the resolution problems in vanadium normalization, but is still a pending issue, regarding the general diffraction measurements.

As a future perspective, the computer code shown in this work will be developed in a user-friendly format, to allow general users to apply it for different systems in diffraction experiments.

9. References

Abdul-Redah, T., Krzystyniak, M. & Chatzidimitriou-Dreismann, C. A. (2005). Neutron compton scattering from water studied with the double-difference technique, *Phys. Rev. B* 72: 052202. URL: *http://link.aps.org/doi/10.1103/PhysRevB.72.052202*

Beckurts, K. & Wirtz, K. (1964). *Neutron Physics, By K.H. Beckurts and K. Wirtz. Translated by L. Dresner*, Springer Verlag OHG Berlin.
URL: *http://books.google.com/books?id=_er8cQAACAAJ*

Bischoff, F. G. (1969). *Generalizad Monte Carlo method for multiple scattering problems in neutron and reactor physics*, PhD thesis, Rensselaer Polytechnic Institute.

Blech, I. A. & Averbach, B. L. (1965). Multiple scattering of neutrons in vanadium and copper, *Phys. Rev.* 137: A1113–A1116.
URL: *http://link.aps.org/doi/10.1103/PhysRev.137.A1113*

Blostein, J. J., Dawidowski, J. & Granada, J. R. (2001). On the analysis of deep inelastic neutron scattering experiments for light nuclei, *Physica B* 304: 357.

Blostein, J. J., Dawidowski, J. & Granada, J. R. (2005). Formalism for obtaining nuclear momentum distributions by the deep inelastic neutron scattering technique, *Phys. Rev. B* 71: 054105.
URL: *http://link.aps.org/doi/10.1103/PhysRevB.71.054105*

Blostein, J. J., Dawidowski, J., Ibáñez, S. A. & Granada, J. R. (2003). Search for anomalous effects in H_2O/D_2O mixtures by neutron total cross section measurements, *Phys. Rev. Lett.* 90(10): 105302.

Blostein, J. J., Rodríguez Palomino, L. A. & Dawidowski, J. (2009). Measurements of the neutron cross sections of hydrogen and deuterium in H_2O/D_2O mixtures using the deep inelastic neutron-scattering technique, *Phys. Rev. Lett.* 102: 097401.
URL: *http://link.aps.org/doi/10.1103/PhysRevLett.102.097401*

Chatzidimitriou-Dreismann, C. A., Abdul Redah, T., Streffer, R. M. F. & Mayers, J. (1997). Anomalous deep inelastic neutron scattering from liquid H_2O/D_2O: Evidence of nuclear quantum entanglement, *Phys. Rev. Lett.* 79: 2839–2842.

Colognesi, D. (2007). Deep inelastic neutron scattering anomalies and quantum decoherence in condensed matter, *Physica B: Condensed Matter* 398 (1): 89–97.

Copley, J. R. D., Verkerk, P., van Well, A. A. & H., F. (1986). Improved monte carlo calculation of multiple scattering effects in thermal neutron scattering experiments, *Computer Physics Communications* 40(2-3): 337 – 357.
URL: *http://www.sciencedirect.com/science/article/pii/0010465586901189*

Cuello, G. & Granada, J. (1997). Thermal neutron scattering by debye solids: A synthetic scattering function, *Annals of Nuclear Energy* 24(10): 763 – 783.
URL: *http://www.sciencedirect.com/science/article/pii/S0306454996000503*

Cuello, G. J. (2008). Structure factor determination of amorphous materials by neutron diffraction, *J. Phys.: Cond. Matter* 20: 244109.

Dawidowski, J. & Cuello, G. J. (2011). Experimental corrections in neutron diffraction of ambient water using h/d isotopic substitution, *Journal of Physics, Conference Series* . In press.

Fischer, H. E., Cuello, G. J., Palleau, P., Feltin, D., Barnes, A. C., Badyal, Y. S. & Simonson, J. M. (2002). D4c: A very high precision diffractometer for disordered materials, *Appl. Phys. A* 74: S160–S162.

Granada, J., Dawidowski, J., Mayer, R. & Gillette, V. (1987). Thermal neutron cross section and transport properties of polyethylene, *Nuclear Instruments and Methods in Physics Research Section A: Accelerators, Spectrometers, Detectors and Associated Equipment* 261(3): 573 – 578.
URL: *http://www.sciencedirect.com/science/article/pii/0168900287903706*

Granada, J. R. (1985). Slow-neutron scattering by molecular gases: A synthetic scattering function, *Phys. Rev. B* 31: 4167–4177.
URL: *http://link.aps.org/doi/10.1103/PhysRevB.31.4167*

Howe, M. A., McGreevy, R. L. & Zetterström, P. (1996). Computer code correct: Correction program for neutron diffraction data. NFL Studsvik.

Kropff, F., Latorre, J. R., Granada, J. R. & Castro Madero, C. (1984). Total neutron cross section of D2O at 20 °C between 0.0005 and 10 ev, *Technical Report EXFOR 30283001*, IAEA.

Lovesey, S. (1986). *The Theory of Neutron Scattering from Condensed Matter*, International series of monographs on physics, Oxford University Press, USA.
URL: *http://books.google.com/books?id=JuupZxrsCTEC*

Mughabghab, S., Divadeenam, M. & Holden, N. (1984). *Neutron Cross Sections: Neutron Resonance Parameters and Thermal Cross Sections*, Neutron Cross Sections Vol. 1, Academic Press. URL: *http://books.google.com/books?id=cgk6AQAAIAAJ*

Paalman, H. H. & Pings, C. J. (1962). Numerical evaluation of X-Ray absorption factors for cylindrical samples and annular sample cells, *J. Appl. Phys.* 33: 2635.

Rodríguez Palomino, L. A., Blostein, J. J. & Dawidowski, J. (2011). Calibration and absolute normalization procedure of a new deep inelastic neutron scattering spectrometer, *Nuclear Instruments and Methods in Physics Research Section A: Accelerators, Spectrometers, Detectors and Associated Equipment* 646(1): 142 – 152.
URL: *http://www.sciencedirect.com/science/article/pii/S0168900211008989*

Rodríguez Palomino, L. A., Dawidowski, J., Blostein, J. J. & Cuello, G. J. (2007). Data processing method for neutron diffraction experiments, *Nuclear Instruments and Methods in Physics Research Section B: Beam Interactions with Materials and Atoms* 258(2): 453 – 470.
URL: *http://www.sciencedirect.com/science/article/pii/S0168583X07003862*

Schmunk, R. E., Randolph, P. D. & Brugger, R. M. (1960). Total cross sections of Ti,V,Y, Ta and W, *Nuclear Science and Engineering* 7: 193–197.

Sears, V. (1975). Slow-neutron multiple scattering, *Advances in Physics* 24(1): 1–45.

Spanier, J. & Gelbard, E. (1969). *Monte Carlo principles and neutron transport problems*, Addison-Wesley series in computer science and information processing, Addison-Wesley Pub. Co. URL: *http://books.google.com/books?id=TP9QAAAAMAAJ*

Squires, G. L. (1978). *Introduction to the theory of thermal neutron scattering*, Cambridge University Press, Cambridge ; New York :.

Neutron Diffraction

Edited by Prof. Irisali Khidirov

Now neutron diffraction is widely applied for the research of crystal, magnetic structure and internal stress of crystalline materials of various classes, including nanocrystalls. In the present book, we make practically short excursion to modern state of neutron diffraction researches of crystal materials of various classes. The book contains a helpful information on a modern state of neutron diffraction researches of crystals for the broad specialists interested in studying crystals and purposeful regulation of their service characteristics, since the crystal structure, basically, defines their physical and mechanical properties. Some chapters of the book have methodical character that can be useful to scientists, interested in possibilities of neutron diffraction. We hope, that results of last years presented in the book, can be a push to new ideas in studying of crystalline, magnetic structure and a macrostructure of usual crystal materials and nanocrystals. In turn, it can promote working out of new materials with new improved service characteristics and to origin of innovative ideas.

How to reference

In order to correctly reference this scholarly work, feel free to copy and paste the following:

J. Dawidowski, G.J. Cuello and L.A. Rodríguez Palomino (2012). Data Processing Steps in Neutron Diffraction: From the Raw Data to the Differential Cross Section, Neutron Diffraction, Prof. Irisali Khidirov (Ed.), ISBN: 978-953-51-0307-3, InTech, Available from: http://www.intechopen.com/books/neutron-diffraction/data-processing-steps-in-neutron-diffraction-from-the-raw-data-to-the-differential-cross-section

INTECH
open science | open minds